RESEARCH PAPER

Mechanical Characterization of Fatigue and Cyclic Plasticity of 304L Stainless Steel at Elevated Temperature

M. Subasic[1] · B. Alfredsson[1] · C. F. O. Dahlberg[1] · M. Öberg[1] · P. Efsing[1,2]

Abstract

Background The mechanical characterization of the cyclic elastoplastic response of structural materials at elevated temperatures is crucial for understanding and predicting the fatigue life of components in nuclear reactors.

Objective In this study, a comprehensive mechanical characterization of 304L stainless steel has been performed including metallography, tensile tests, fatigue tests, fatigue crack growth tests and cyclic stress-strain tests.

Methods Isothermal tests were conducted at both room temperature and 300 °C for both the rolling direction and the transverse direction of the hot rolled steel. Mechanical properties were extracted from the uniaxial experiments by fitting relevant material models to the data. The cyclic plasticity behavior has been modelled with a radial return-mapping algorithm that utilizes the Voce nonlinear isotropic hardening model in combination with the Armstrong-Frederick nonlinear kinematic hardening model. The plasticity models are available in commercial FE software and accurately capture the stabilized hysteresis loops, including a substantial Bauschinger effect.

Results The material exhibits near isotropic properties, but its mechanical performance is generally reduced at high temperatures. Specifically, in the rolling direction, the Young's modulus is reduced by 16 % at 300 °C, the yield strength at 0.2 % plastic strain is lower by 23 %, and the ultimate tensile strength is lower by 30 % compared to room temperature. Fatigue life is also decreased, leading to an accelerated fatigue crack growth rate compared to room temperature. A von Mises radial return mapping algorithm proves to be effective in accurately modelling the cyclic plasticity of the material. The algorithm has also been used to establish a clear correlation between energy dissipation per cycle and cycles to failure, leading to the proposal of an energy-based fatigue life prediction model.

Conclusions The material exhibits reduced mechanical performance at elevated temperatures, with decreased monotonic strength, compared to room temperature. Fatigue life is also compromised, resulting in accelerated fatigue crack growth. The material's hardening behavior differs at room temperature and elevated temperature, with lower peak stress values observed at higher temperatures. The radial return mapping algorithm can be used to determine the dissipated energy per cycle which together with fatigue testing has been used to propose a low cycle fatigue life prediction model at both temperatures.

Nomenclature

a	radius of the smallest cross-section
a_0	initial radius of cross-section
b	fatigue strength exponent
C	Paris law parameter
c	fatigue ductility exponent
C_k	kinematic hardening modulus
da/dN	crack growth rate
E	Young's modulus
F	geometry function
f	yield surface
$H\prime$	cyclic strength coefficient
N_f	fatigue life
n	Paris law exponent
n_i	number of tests on level i
$n\prime$	cyclic strain hardening exponent
P	force on specimen
p	power law exponent

✉ M. Subasic
  msubasic@kth.se

1 Solid Mechanics, Department of Engineering Mechanics, KTH Royal Institute of Technology, SE-100 44 Stockholm, Sweden

2 Ringhals AB, Ringhalsverket, SE-432 85 Väröbacka, Sweden

p_i	failure probability on level i
q	back stress
$\dot{q}$	back stress increment
R	load ratio
r	radius of curvature of the neck
r_i	number of runouts on level i
t	specimen thickness
W	dissipated energy density per cycle
W_a	energy density parameter
W_b	energy density parameter
w	specimen characteristic length
X_i	normally distributed stochastic variable
α	accumulated plastic strain
$\dot{\alpha}$	accumulated plastic strain increment
β	isotropic saturation exponent
γ_{k}	kinematic hardening parameter
ΔK_I	mode I stress intensity range
$\Delta \varepsilon$	strain increment
$\Delta \lambda$	Lagrange (plastic) multiplier
δ	imperfection
ε	uniaxial true strain
ε_a	strain amplitude
ε_e	fatigue limit
ε^e	elastic strain
ε_f'	fatigue ductility coefficient
ε_i	strain amplitude on level i
ε^p	plastic strain
$\dot{\varepsilon}^p$	plastic strain increment
ε_{50}	strain amplitude level with $p = 0.5$
λ	consistency parameter
ξ	auxiliary variable (relative stress)
ρ	density
σ	uniaxial true stress
σ_a	stress amplitude
σ_f'	fatigue strength coefficient
σ_{sat}	isotropic saturation flow stress
σ_{Y0}	monotonic yield stress
σ_{Y}	cyclic yield stress
σ_{ε_e}	standard deviation for fatigue limit

Acronyms

ASTM	American society for testing and materials
CT	compact tension
EDM	electrical discharge machining
FE	finite element
FEM	finite element method
LOM	light optical microscope
LTO	long term operation
RD	rolling direction
RT	room temperature
STD	short transverse direction
TD	transverse direction

Introduction

Fatigue due to large amplitude cyclic loading is important in many engineering applications, such as the nuclear power industry, where low cycle fatigue can occur due to thermal fluctuations or mechanically induced vibrations. This is a problem in many components, such as at mixing points in the main piping systems where hot and cool water is mixed. The temperature fluctuations at the mixing points give rise to varying temperature loads. The mechanical properties of a material can differ significantly at elevated temperatures, which emphasizes the need for mechanical characterizations of fatigue and cyclic plasticity properties at different temperatures. There is an ongoing global long-term operation (LTO) program for nuclear power plants that aims to ensure the safe and efficient operation of nuclear reactors beyond their original design lifetimes. This program involves comprehensive assessments and maintenance to extend the operational lifespan of existing nuclear power plants from 40 years to 60 years or even up to 80 years. Hence, fatigue assessments of nuclear materials at different temperatures are a vital part of the LTO program in order to maintain the generation of clean and reliable electricity while prioritizing safety and sustainability [1].

Coffin and Manson [2, 3] were the first researchers to model the Wöhler or S-N curves by relating the number of cycles to failure to the plastic strain amplitude. Basquin [4] provided a similar model in which the number of cycles to failure is instead related to the elastic strain amplitude. The Basquin and Coffin-Manson models together form the well-known strain-life equation, which describes the fatigue performance of a material. In this equation, the elastic and plastic strain amplitudes combine to form the total strain amplitude. Ramberg and Osgood [5] also implemented an additive decomposition of the total strain amplitude into an elastic and plastic part to describe its relation to the stress amplitude. This model describes the shape of the cyclic stress-strain curve, which is obtained from the stabilized hysteresis loops of fully reversed strain-controlled loading. Paris et al. [6] suggested a rule known as the Paris law, which describes the fatigue crack growth rate as a function of the stress intensity factor. This equation holds in the "mid-growth" range, known as Region II, of the crack growth curve and can be used to model the fatigue crack growth rates.

Cyclic plastic deformation is a complicated process and several constitutive models have been developed to capture the phenomena of interest, such as the Bauschinger effect, ratcheting and saturation of hysteresis loops. Prager [7] provided a phenomenological model for kinematic hardening used to represent the hardening behavior in metals under

cyclic loading. The model predicts the translation of the center of the yield surface, which is experimentally observed to occur in the direction of the plastic flow. Ziegler [8] further improved the model and constructed an evolution law that captures the aforementioned effect by introducing an internal variable called back stress, which defines the location of the center of the yield surface. The Prager-Ziegler rule assumes a constant kinematic hardening modulus. However, metals subjected to cyclic loading usually exhibit nonlinear strain hardening behavior. Additionally, the yield surface not only translates but also changes in size, a phenomenon known as isotropic hardening. Thus, a kinematic hardening model is generally used in conjunction with an isotropic hardening model to obtain a mixed formulation that correctly captures the real response of the material. Voce [9] proposed a nonlinear isotropic hardening law in which a saturation hardening term of the exponential type is appended to the yield strength, defining the initial size of the yield surface. Mroz [10] generalized the Prager rule to develop a nonlinear kinematic hardening model based on a multilinear response. In this model, a linear kinematic hardening law is adopted for each linear part of the response, successfully expressing phenomena such as cyclic relaxation and cyclic creep, also known as ratcheting. Another multilinear kinematic hardening rule is the one developed by Ohno and Wang [11]. Frederick and Armstrong [12] also proposed a nonlinear kinematic hardening model in which a strain-memory term, also known as the dynamic recovery term, is added to Melan-Prager's linear hardening rule. This term introduces nonlinearity to the model and provides a more accurate prediction of the Bauschinger effect. The model has been enhanced in various ways by many researchers to predict more complex material behavior [13]. The most well-known development and improvement of the Armstrong-Frederick model is the generalization introduced by Chaboche [14]. This generalization is based on the superposition of several nonlinear kinematic hardening rules. The purpose of this development was to improve a large overestimate of ratcheting effects and to allow for greater flexibility in the model [13].

The aim of this study is to provide a comprehensive mechanical characterization of the fatigue properties and cyclic elastoplastic response of 304L. Fatigue and cyclic plasticity have been widely investigated at different temperatures before [2, 14–32], but the availability of the hardening parameters at elevated temperatures is limited due to the notorious problem of buckling at high strain amplitudes.

A return mapping algorithm is introduced for the modelling of cyclic plasticity in 304L stainless steel at elevated temperature. By considering the cyclic plasticity behavior and conducting fatigue testing, the algorithm allows for the prediction of the material's low cycle fatigue life using an energy dissipation approach. Hence, this paper offers insights that are particularly relevant to the nuclear power industry, given the ongoing global long-term operation programs for nuclear reactors operating under cyclic loading conditions at elevated temperatures. The findings presented in this paper will be valuable for assessing the durability and performance of such reactors to ensure the maintenance of fossil-free electricity production.

Material and methods

The material used is a 304L stainless steel plate that originated from the manufacturing of the now decommissioned nuclear power plant Barsebäck in Sweden. Grade 304L is an austenitic chromium-nickel stainless and heat resistant steel with high toughness even at cryogenic temperatures due to its austenitic structure. It is widely used in automotive, machinery and nuclear engineering fields due to its excellent combination of strength, ductility and corrosion resistance. Type 304L is the low carbon version of type 304, which makes it less prone to sensitization and reduces susceptibility to intergranular stress corrosion cracking. The chemical composition of the material is presented in Table 1.

Experimental procedure

The experimental testing is performed under isothermal conditions at both room temperature and 300 °C by use of a servo-hydraulic testing machine. A furnace was installed in the testing machine for the elevated temperature tests and a thermocouple was placed on a dummy specimen in the furnace to control the temperature. The choice of the elevated temperature is based on the average operating temperature in the piping system of nuclear reactors. The isotropy of the material has been investigated by manufacturing specimens in both the rolling direction and the transverse direction of the hot rolled steel. Round bar specimens with a uniform gauge length are used for the tensile tests, fatigue tests and cyclic stress-strain tests. The fatigue crack growth tests are conducted with CT specimens. All test specimens

Table 1 Chemical composition (% by mass) of the 304L stainless steel plate

C	Si	Mn	P	S	Cr	Ni	Nb	Co	N
0.04	0.52	1.09	0.019	0.014	17.5	9.3	0.57	0.028	0.033

Fig. 1 The geometries of the test specimens

CT specimen

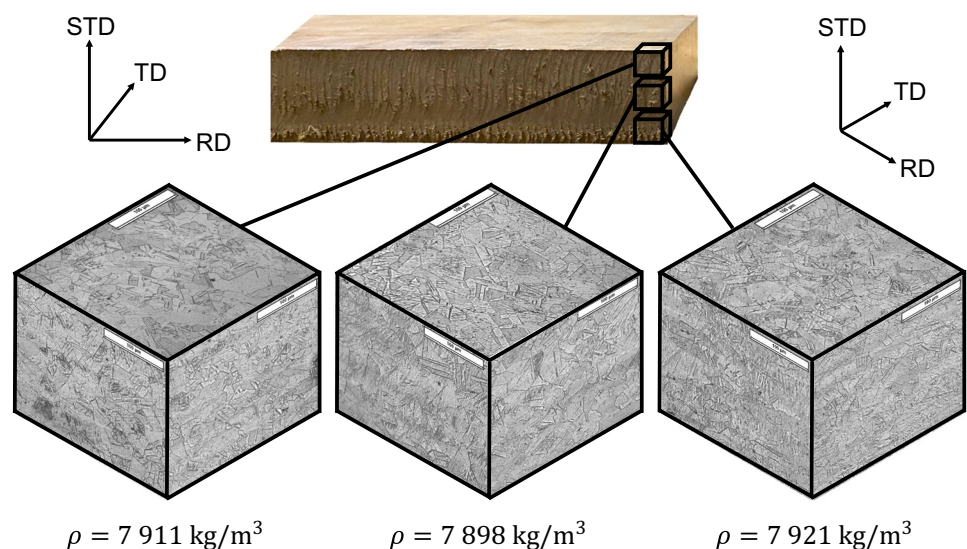Tensile test specimen

Cyclic test specimen

Fatigue test specimen
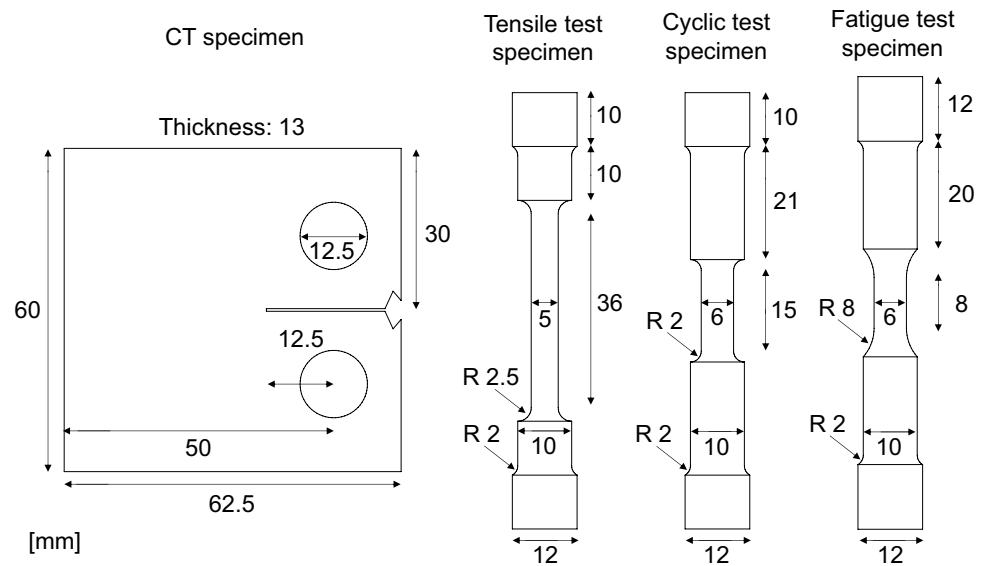
are manufactured using EDM and the geometries are illustrated in Fig. 1.

Metallography

The cross-thickness homogeneity of the plate was investigated to ensure that all test specimens are homogeneous. Density measurements, using Archimedes' principle, were performed on three small cubes along the thickness direction. The densities of the cubes along the thickness are shown in Fig. 2 and all measurements correspond well with the density of 7 900 kg/m^3 for 304L stainless steel [33]. The homogeneity and isotropy of the material were investigated through metallography on polished and

etched samples taken along the thickness of the plate. The specimens were etched in a mixture of hydrochloric and nitric acid diluted with water and heated to 50 °C. The samples were immersed in the fluid for a few seconds and the surfaces were studied using light optical microscopy (LOM) to analyze the grains. This analysis was performed in the rolling direction, transverse direction and short transverse direction of the material at three different positions along the thickness of the plate. The grains are approximately 30 μm in size, and the grain boundaries, shown in Fig. 2, are similar in all directions and positions of the plate. Hence, the material exhibits high isotropy and homogeneity in the plate with respect to microstructure.

Fig. 2 The microstructure and densities of the 304L stainless steel along the thickness of the plate in the rolling direction (RD), transverse direction (TD) and short transverse direction (STD)

$\rho = 7\,911$ kg/m^3 $\rho = 7\,898$ kg/m^3 $\rho = 7\,921$ kg/m^3

Tensile tests

The tensile tests were conducted according to ASTM E8 [34] by gradually elongating the specimens with displacement control at a rate of 0.015 mm/s. The resulting load was captured as a function of the strain, which was measured by use of extensometers. Two extensometers were diametrically mounted onto the gauge section of the specimen to account for any misalignments. Inhomogeneous deformation occurred in the material prior to failure in the form of necking. A camera setup was installed in front of the servo-hydraulic testing machine to capture pictures of the neck. The pictures were then analyzed using ImageJ to extract the radius of curvature in the necking region and Bridgman correction for the multiaxial stress was employed. For the tests at elevated temperature, a FEM inverse modelling procedure [35] was employed to compute the true axial stress and strain records in the post peak load regime instead of the Bridgman correction since the camera setup could not be used in the furnace. This involved iteratively aligning finite element solutions with the experimental test data. The initiation of necking was regulated by reducing the linear dimensions of the specimen's central cross-section by a factor of 1-δ, where δ can be considered as an imperfection. All tensile test specimens were intentionally introduced with a manufactured imperfection matching $\delta \approx 0.004$, which was also incorporated into the finite element models.
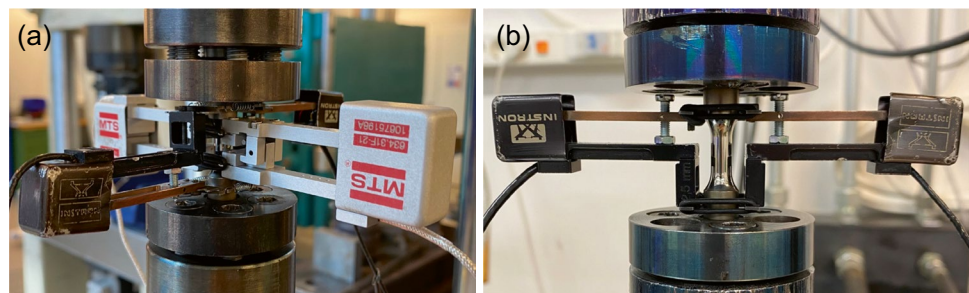
Fatigue tests

The fatigue tests were performed according to ASTM E-606 [36] with fully reversed cyclic loads ($R = -1$) at constant strain amplitudes. The tests were strain controlled by use of two extensometers diametrically mounted onto the section of the specimen where the diameter is 10 mm, see Fig. 3(b). The extensometers were not directly attached to the gauge section to avoid scratching the polished surface with their sharp edges, as this could serve as a crack initiation site and influence the fatigue life. The majority of the strain is localized in the gauge section of the specimen. Thus, the extensometer distance of 25 mm, which

is longer than the length of the gauge section, cannot be used to calculate the strain accurately. Using this distance would underestimate the actual strain in the specimen. Hence, extensometer comparison testing has been performed to determine the correct strain in the gauge section, see Fig. 3(a). The tests were conducted at various strain amplitudes using two pairs of extensometers: one pair on the thicker section and another pair attached to the gauge section. The tests were strain-controlled with the extensometer pair attached to the thicker section while the other extensometer pair measured the strain in the gauge section. As a result, a relationship between the strain amplitudes from the two pairs of extensometers was established for all intended strain amplitudes to be used in the fatigue testing. The strain amplitude conversion was then adopted for the fatigue tests at both room temperature and 300 °C. The surface of the fatigue test specimens, shown in Fig. 1, was polished in the gauge section to a surface finish of 0.15 µm (Ra), as measured with a white light interferometry (WLI) microscope. The fatigue tests were conducted at a frequency of 10 Hz. Typically, force controlled testing is used for high cycle fatigue to determine the fatigue limit, as it allows for higher frequencies. However, force controlled testing in this case resulted in ratchetting and unreasonably low fatigue life due to high accumulated plastic strains. This was caused by a fatigue limit close to the yield strength of the material, leading to strain hardening and significant plastic dissipation. Consequently, force controlled testing could not be used and displacement control was employed for both the high cycle and low cycle fatigue regions.

Two-point testing [37, 38] was used to determine the fatigue limit. Fatigue tests were performed at two strain levels, one slightly above and one slightly below the fatigue limit. The chosen strain levels were designed to encompass the fatigue limit while still being close enough to induce both failure and runouts. A specimen was considered to have reached a run-out when it reached two million cycles and the test was then terminated. A total of 16 specimens were used for the two-point testing, with four specimens at each strain level for both temperature conditions.

Fig. 3 (a) Extensometer comparison for strain amplitude and (b) experimental setup for fatigue testing

Fatigue crack growth tests

The fatigue crack growth tests were conducted according to the ASTM E-647 standard [39] with CT specimens, see Fig. 1. The load cycles were pulsating with an R-ratio slightly above but close to zero. A zero minimum stress was avoided due to practical reasons. The tests were controlled by the stress intensity range which started at 15 MPa $\sqrt{\text{m}}$ and gradually increased to 40 MPa $\sqrt{\text{m}}$. The crack growth rate was then calculated from the crack mouth opening displacement which was measured with clip gauges mounted to the CT specimens.

Cyclic stress-strain tests

The cyclic stress-strain tests were conducted using the cyclic test specimens, as shown in Fig. 1. Two extensometers were diametrically mounted onto the gauge section. The specimen was loaded with an alternating strain amplitude ($R = -1$) until a stabilized hysteresis loop was obtained. The maximum number of cycles required for the hysteresis loop to stabilize was below 20 cycles. The strain amplitude was controlled through the extensometers and gradually increased for the same specimen until failure. Since buckling is a problem when performing large amplitude cyclic tests at high temperatures, the diameter was increased to 7 mm for the tests at 300 °C. In addition, the furnace could not be used at elevated temperatures because the setup in the testing machine, with the long and small shafts passing through the furnace, was too weak to resist buckling in the specimen. Instead, heat lamps were used around the specimen along with a more rigid setup in the testing machine.

Material modelling

The mechanical tests are modelled to determine the mechanical properties of the homogeneous and isotropic material. An associative flow rule suffices since we have plastic incompressibility and purely deviatoric plastic strain rates for metals and steel. The modelling of the mechanical tests will therefore be limited to the classical elastoplastic von Mises material model.

Monotonic stress-strain curve

A monotonic stress-strain curve is obtained from the uniaxial tensile tests in which the Young's modulus, yield strength and ultimate tensile strength can be determined. The monotonic yield stress, σ_{Y0}, was determined at 0.2 % plastic strain. A neck is formed in the specimen at the end of the test, resulting in a multiaxial stress state. Bridgman [40] developed a

correction formula for the axial stress that considers the 3D stress state in the neck. The equation is given by

$$\sigma = \frac{P}{\pi a^2 \left(1 + \frac{2r}{a}\right)\ln\left(1 + \frac{a}{2r}\right)},\tag{1}$$

where P is the force, a is the radius of the smallest cross-section in the neck and r is the radius of curvature of the neck. The effective strain is computed as

$$\varepsilon = 2\ln\frac{a_0}{a},\tag{2}$$

where a_0 is the initial radius of the cross-section. The geometry parameters were determined using digital analyses of close-up pictures with the software ImageJ. The assumptions made in the analysis by Bridgman, considering the conditions in the neck, include axisymmetry, incompressibility and the assumption that the longitudinal strain component is constant over the smallest cross-section of the neck. These assumptions were based on experimental observations. Davidenkov and Spiridonova [41] presented a similar investigation on the necking problem, but the Bridgman correction is the most common one. Voce law can be used to model the relationship between the monotonic stress and strain according to

$$\sigma = \sigma_{Y0} + \sigma_{\text{sat}}\left[1 - \exp(-\beta\varepsilon)\right],\tag{3}$$

where σ_{Y0} is the monotonic yield strength and σ_{sat} and β are fitting parameters.

Fatigue crack growth rate

The fatigue crack growth rate is modelled with the Paris law

$$\frac{\mathrm{d}a}{\mathrm{d}N} = C\left(\Delta K_I\right)^n.\tag{4}$$

Here, C and n are material parameters which were determined by the least squares fit to the stress intensity range, ΔK_I, and the crack growth rate, $\mathrm{d}a/\mathrm{d}N$, data. The stress intensity range is given by

$$\Delta K_I = \frac{\Delta P}{tw^{1/2}}F,\tag{5}$$

where ΔP is the force range, t is the thickness, w is the 50 mm length shown in Fig. 1 for the CT specimen and F is a geometry function commonly found in solid mechanics handbooks.

S-N curves

The fatigue life is modelled with the Coffin-Manson-Basquin strain-life equation given by

$$\varepsilon_a = \frac{\sigma_f'}{E}\left(2N_f\right)^b + \varepsilon_f'\left(2N_f\right)^c, \tag{6}$$

where ε_a is the strain amplitude, σ_f' is the fatigue strength coefficient, b is the fatigue strength exponent, ε_f' is the fatigue ductility coefficient and c is the fatigue ductility exponent. All fatigue data points above the fatigue limit were fitted to Eq. (6) with the least squares method.

The test outcome from the two-point testing is used to determine the strain amplitude level at a 50 % failure probability, which is then utilized to estimate the fatigue limit. All test results for the selected lower and upper strain levels, ε_1 and ε_2 respectively, are included for computing the fatigue limit, while the test results for other strain amplitudes are discarded. The failure probability on each level is given by

$$p_i = \frac{n_i - r_i}{n_i}, \tag{7}$$

where n_i is the total number of tests and r_i is the number of runouts on each level $i \in (1,2)$. If only runouts were achieved for ε_1, then a fictive value for p_1 is used where $p_1 = 1/(2n_1)$. Similarly, if only failures were achieved for ε_2, then $p_2 = 1 - 1/(2n_2)$. The failure probability p_i is approximately normally distributed with the sampled failures at ε_i. Thus, a normally distributed stochastic variable X_i can be used for determining the fatigue limit. The median strain ε_{50} is determined by linear interpolation of strains ε_i on the variable X,

$$\varepsilon_{50} = \varepsilon_1 - X_1 \frac{\left(\varepsilon_2 - \varepsilon_1\right)}{\left(X_2 - X_1\right)}. \tag{8}$$

The mean value of the normal distribution is assumed to be equivalent to the material fatigue limit, ε_e, which is expected to agree with ε_{50}. The standard deviation for the fatigue limit,

$$\sigma_{\varepsilon_e} = \frac{\varepsilon_2 - \varepsilon_1}{X_2 - X_1}, \tag{9}$$

follows from the two points on the normal distribution.

Cyclic plasticity

A cyclic stress-strain curve can be modelled with the Ramberg-Osgood model

$$\varepsilon_a = \frac{\sigma_a}{E} + \left(\frac{\sigma_a}{H'}\right)^{1/n'}, \tag{10}$$

to obtain the relationship between strain amplitude and stress amplitude. Here, n' is the cyclic strain hardening exponent and H' is the cyclic strength coefficient.

A numerical implementation of one-dimensional plasticity has been utilized to model the cyclic plasticity behavior of the material. Classical rate-independent plasticity is adopted with the phenomenological strain hardening models known as isotropic and kinematic hardening. The elastic response is modelled with Hooke's law

$$\sigma = E(\varepsilon - \varepsilon^p), \tag{11}$$

where an additive decomposition of the total strain, ε, into an elastic and plastic part, ε^e and ε^p, respectively, is here assumed,

$$\varepsilon = \varepsilon^e + \varepsilon^p. \tag{12}$$

The evolution equation for the plastic strain is given by the flow rule

$$\dot{\varepsilon}^p = \lambda \, \text{sign}(\sigma), \tag{13}$$

where

$$\text{sign}(\sigma) = \begin{cases} +1 \text{ if } \sigma > 0 \\ -1 \text{ if } \sigma < 0 \end{cases}, \tag{14}$$

and λ is the magnitude of the plastic strain increment, also known as the consistency parameter. The nonlinear isotropic hardening model by Voce is adopted to describe the expansion of the yield surface according to

$$H(\alpha) = \sigma_Y + \sigma_{\text{sat}}\left[1 - \exp(-\beta\alpha)\right], \tag{15}$$

where σ_Y is the cyclic yield strength of the material and thus the initial size of the yield surface. Here, σ_{sat} is the saturation flow stress describing the final size of the yield surface while β is the hardening rate which determines how fast the yield surface saturates. The variable α is a nonnegative internal hardening variable and a function of the amount of plastic flow (slip). It is commonly referred to as the accumulated plastic strain with the evolution equation

$$\dot{\alpha} = |\dot{\varepsilon}^p|. \tag{16}$$

By recalling Eq. (13), we realize that $\dot{\alpha} = \lambda$. The nonlinear kinematic hardening model proposed by Armstrong and Frederick is implemented in conjunction with the isotropic hardening law by introducing an additional internal variable, denoted by q and called back stress, with the evolution law

$$\dot{q} = \frac{2}{3}C_k\dot{\varepsilon}^p - \gamma_k\dot{\alpha}q. \tag{17}$$

In Eq. (17), C_k characterizes the kinematic hardening modulus while γ_k is a nondimensional material parameter characterizing nonlinear kinematic hardening behavior. Considering the introduced internal hardening variable q, which defines the location of the center of the yield surface, the flow rule in Eq. (13) can now be modified to the form

$$\dot{\varepsilon}^p = \lambda \, \text{sign}\left(\sigma - \frac{3}{2}q\right). \tag{18}$$

The governing equations of a J_2 material model is considered and a von Mises yield criterion is consequently adopted in the form

$$f(\sigma, q, \alpha) = \left|\sigma - \frac{3}{2}q\right| - \left(\sigma_Y + \sigma_{sat}[1 - \exp(-\beta\alpha)]\right). \quad (19)$$

The irreversible nature of plastic flow is captured by means of the Karush-Kuhn-Tucker complementarity conditions which in the present context read

$$\lambda \geq 0, \ f(\sigma, q, \alpha) \leq 0, \ \lambda f(\sigma, q, \alpha) = 0, \quad (20)$$

Table 2 Return mapping algorithm for 1D nonlinear isotropic and kinematic hardening

Initial conditions:
$$\varepsilon_n^p = 0$$
$$\alpha_n = 0$$
$$q_n = 0$$

Elastic predictor:
$$\varepsilon_{n+1} = \varepsilon_n + \Delta\varepsilon_n$$
$$\sigma_{n+1}^{trial} = E(\varepsilon_{n+1} - \varepsilon_n^p)$$
$$\xi_{n+1}^{trial} = \sigma_{n+1}^{trial} - \frac{3}{2}q_n$$
$$f_{n+1}^{trial} = \left|\xi_{n+1}^{trial}\right| - (\sigma_Y + \sigma_{sat}[1 - \exp(-\beta\alpha_n)])$$

IF $f_{n+1}^{trial} \leq 0$ THEN
$$\sigma_{n+1} = \sigma_{n+1}^{trial}$$
ELSE
Solve $f_{n+1} = 0$ for $\Delta\lambda$

WHILE abs(f) > TOLERANCE

Newton-Raphson iteration
See **Appendix C**

END WHILE

$$\text{sign}(\xi_{n+1}) = \frac{\xi_{n+1}^{trial} + \left(1 - \frac{1}{1+\gamma_k\Delta\lambda}\right)\frac{3}{2}q_n}{\left|\xi_{n+1}^{trial} + \left(1 - \frac{1}{1+\gamma_k\Delta\lambda}\right)\frac{3}{2}q_n\right|}$$

$$\sigma_{n+1} = \sigma_{n+1}^{trial} - \Delta\lambda E \, \text{sign}(\xi_{n+1})$$

$$\varepsilon_{n+1}^p = \varepsilon_n^p + \Delta\lambda \, \text{sign}(\xi_{n+1})$$

$$q_{n+1} = \frac{1}{1+\gamma_k\Delta\lambda}q_n + \frac{2}{3}\frac{1}{1+\gamma_k\Delta\lambda}C_k\Delta\lambda \, \text{sign}(\xi_{n+1})$$

$$\alpha_{n+1} = \alpha_n + \Delta\lambda$$

END IF

and represent the loading-unloading conditions for plasticity. The consistency parameter, λ, is determined from the consistency condition

$$\lambda\dot{f}(\sigma, q, \alpha) = 0. \quad (21)$$

The energy dissipation increment for each strain step can be computed as

$$W_i = |\sigma_{n+1}|\lambda, \quad (22)$$

where σ_{n+1} is the updated stress. The total energy dissipation per cycle is then given by

$$W = \sum_{i=1}^{m} W_i, \quad (23)$$

where m is the number of solution steps in one cycle. A discrete formulation of the constitutive models may be expressed by applying an implicit backward Euler integration scheme, see Appendix A. This leads to the classical return-mapping algorithm originally proposed by Wilkins [42] and further developed by Simo and Hughes [43] among others. It is worth emphasizing that the algorithmic procedure is more complicated in the present context of plasticity with nonlinear kinematic hardening. This is attributed to the fact that the sign of the auxiliary variable is a function of the consistency parameter and needs to be determined, see Appendix B, in contrast to the standard case of plasticity with linear kinematic hardening which is more straight forward [44]. The return-mapping algorithm is then completed with an iterative Newton-Raphson method, see Appendix C, and can be implemented in Matlab. The numerical algorithm is for convenience summarized in Table 2.
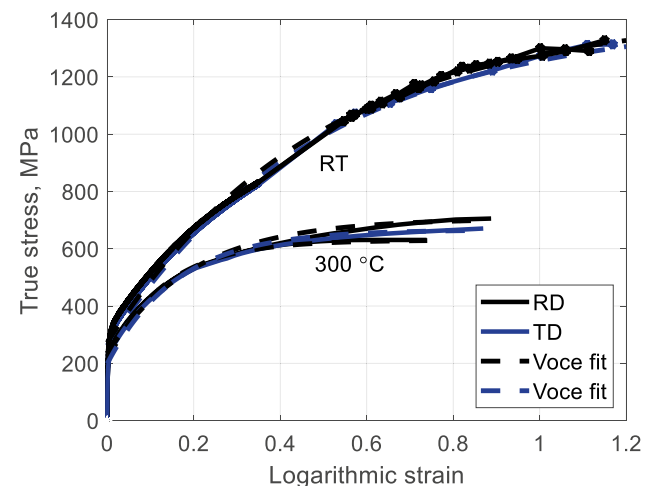
Fig. 4 Monotonic stress-strain curves

Table 3 Mechanical properties and Voce parameters

|		E GPa	σ_{Y0} MPa	σ_{UTS} MPa	σ_{sat} MPa	β
RT	RD	194	272	627	1150	2.08
	TD	166	262	625	1140	2.06
300 °C	RD	163	209	439	421	7.51
	TD	151	199	434	467	6.20

Results

Tensile tests

The monotonic stress-strain curves obtained from the uniaxial tensile tests are shown in Fig. 4. The material demonstrates substantial ductility with a logarithmic strain of up to 1.2 at room temperature. The material exhibits less hardening and ductility at elevated temperature. The mechanical properties obtained by the tensile tests and the Voce fit parameters are listed in Table 3.

Fatigue tests

The fatigue test results are illustrated in Fig. 5 with corresponding Basquin-Coffin-Manson parameters in Table 4. The fatigue life is slightly shorter at elevated temperature compared to room temperature.

The fatigue limits are illustrated in Fig. 6 at room temperature and 300 °C. A fatigue limit of 1.540×10^{-3} in strain amplitude was obtained at room temperature and 1.485×10^{-3} at 300 °C. The standard deviation of the fatigue limit is 4.9×10^{-5} and 4.3×10^{-5} at room temperature and 300 °C, respectively.
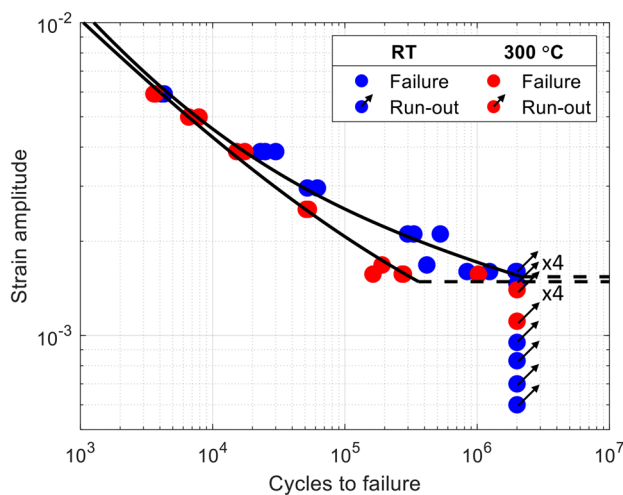
Fatigue crack growth tests

The crack growth test results are shown in Fig. 7. The material displays high isotropy in terms of crack growth as well. Once again, the 304L stainless steel exhibit slightly weaker properties at elevated temperature with faster crack growth rates. The Paris law parameters are presented in Table 5.

Cyclic stress-strain tests

The hysteresis loops at room temperature are illustrated in Fig. 8. High isotropy is displayed by the material for the cyclic stress-strain curves as well. The hysteresis loop stabilized quickly for lower strain amplitudes while at higher amplitudes, more cycles were required to achieve a stabilized loop. However, the hysteresis loop stabilized before reaching 20 cycles for all strain amplitudes. Isotropy is also evident for the hysteresis loops at 300 °C, see Fig. 9. The curves flatten down and do not harden as much at higher strain amplitudes. On the contrary, the specimens survived up to an impressive strain range of 4 % before failure. The results show higher isotropic hardening at elevated temperature. Otherwise, the hardening is similar to room temperature with a clear Bauschinger effect.

The cyclic stress-strain curve is formed by a line from the origin that passes through the tips of the stabilized hysteresis loops. This is illustrated in Fig. 10. The curves can be fitted to the Ramberg-Osgood model in Eq. (10) to obtain the relationship between stress and strain amplitude, see Table 6. The Young's modulus is taken from the tensile test results in Table 3. The monotonic stress-strain curves from the tensile tests can also be used to compare with the cyclic stress-strain curves. The material displays substantial cyclic hardening at both room temperature and 300 °C since the cyclic curves are clearly above the monotonic tension curves.

Fig. 5 Fatigue test results at room temperature and 300 °C

Table 4 Basquin-Coffin-Manson parameters

		σ_f' MPa	b	ε_f'	c
RD	RT	1500	-0.109	0.727	-0.598
	300 °C	300	-0.062	0.253	-0.438
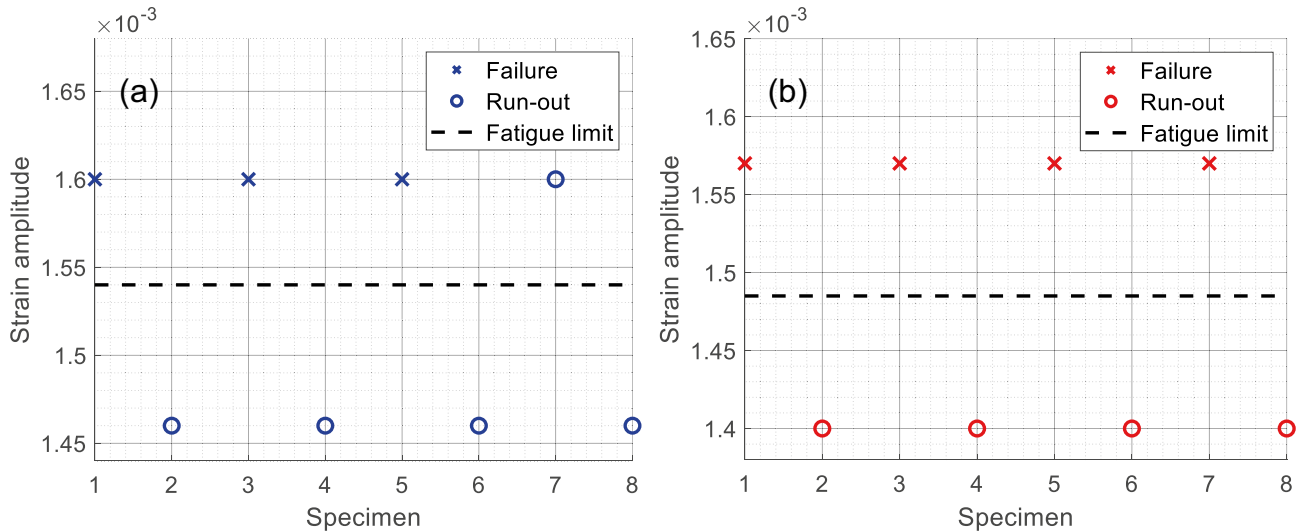
Fig. 6 Fatigue limit at (**a**) room temperature and (**b**) 300 °C determined by two-point testing

The cyclic hardening exhibited by the material can be modelled by implementing the Armstrong-Frederick nonlinear kinematic hardening model shown in Eq. (17) in conjunction with the Voce nonlinear isotropic hardening model in Eq. (15). The results are illustrated in Fig. 11 at room temperature and in Fig. 12 at 300 °C. The kinematic and isotropic hardening parameters for both conditions are presented in Table 7 and Table 8, respectively.

The dissipated energy per cycle was determined by analysing the stabilized hysteresis loop for each fatigue test conducted in the low cycle fatigue region. The energy dissipation was computed utilizing the return mapping algorithm, considering the hardening parameters derived from the cyclic tests. The obtained results exhibited a noticeable correlation between the energy dissipation per cycle, denoted as W, and the corresponding fatigue life, N_f, as

shown in Fig. 13. Consequently, an energy-based fatigue life prediction model can be developed by employing a power law fit given by

$$W = W_a\left(N_f\right)^p + W_b, \tag{24}$$

where W_a and W_b are energy density parameters while p is a power law exponent. The three parameters at both room temperature and 300 °C are listed in Table 9.
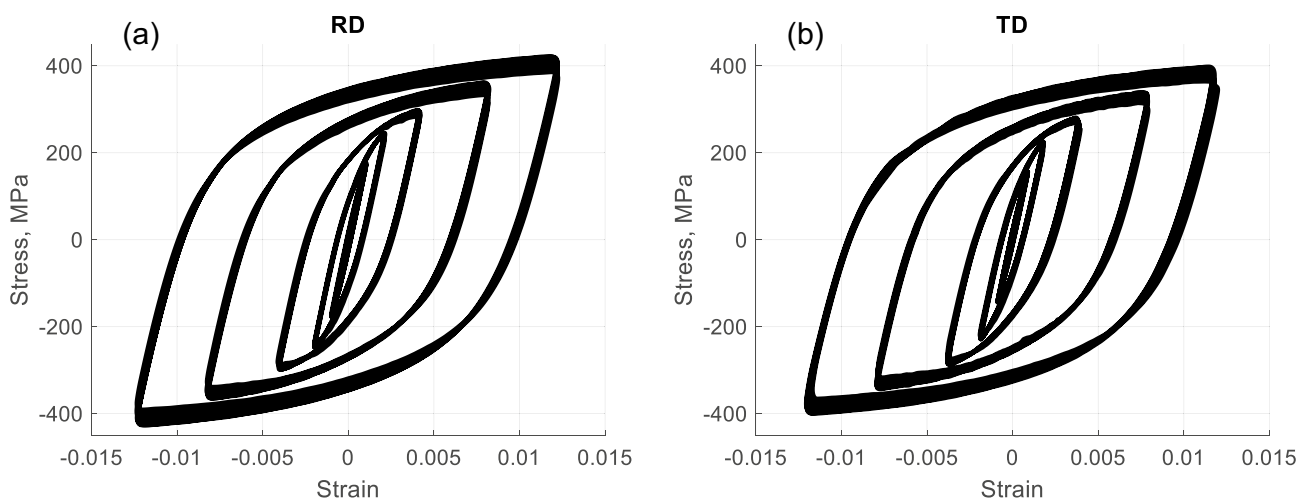
Discussion

In the tensile tests, an elastic anisotropy at room temperature is evident where the Young's modulus in the transverse direction is 14 % lower compared to the rolling direction. This indicates the possibility of some texture in the material toward the rolling direction, despite the presence of equiaxed grains shown in Fig. 2. At 300 °C, the elastic anisotropy is lowered to a 7 % difference between the rolling and transverse directions. Regarding plastic deformation, the material exhibits high isotropy in both the rolling and transverse directions at both temperatures.
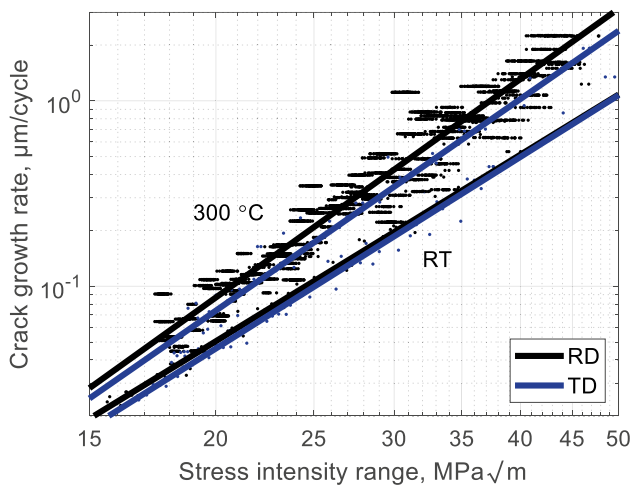
Fig. 7 Crack growth rates at room temperature and 300 °C

Table 5 Paris law parameters

|		C $\left[\dfrac{\text{m/cycle}}{\left(\text{MPa}\sqrt{\text{m}}\right)^n}\right]$ 10^{-12}	n
RT	RD	2.253	3.344
	TD	1.572	3.434
300 °C	RD	0.702	3.915
	TD	0.859	3.793

Fig. 8 Hysteresis loops at room temperature for different strain amplitudes in (**a**) the rolling direction (RD) and (**b**) the transverse direction (TD)

The Basquin-Coffin-Manson model fit shows an approximately linear curve fit for the fatigue tests at 300 °C while the fitted curve for the tests at room temperature is clearly nonlinear, see Fig. 5. This indicates that plastic flow is present in the material even in the high cycle fatigue region at 300 °C. In contrast, the nonlinear S-N curve at room temperature indicates that the loads primarily exhibit elasticity in the high cycle fatigue region, close to the fatigue limit. This is attributed to the fact that the yield strength is higher at room temperature. Thus, it can be concluded that the material demonstrates impressive fatigue limits for both conditions since they are very close to the yield strengths. This is also the reason behind performing strain-controlled fatigue testing for the entire S-N curve since force-controlled testing resulted in ratcheting, which quickly broke the specimens due to the high accumulation of plastic strain. Considering

the fatigue limits in Fig. 6, a fictive value had to be used for three out of four strain levels to estimate the failure probability since only failures or runouts were observed at these levels. A better approximation of the fatigue limit would be obtained if more specimens were used or if the two strain amplitude levels were closer to each other.

The cyclic elastoplastic response was mainly dominated by kinematic hardening initially for the lower strain amplitudes with subsequent isotropic hardening at high strain amplitudes for both temperatures. The material exhibits a clear Bauschinger effect where compressive yielding in the reverse direction commences already in tension, see Figs. 8 and 9. This is attributed to the high kinematic hardening and the fact that metals and steel consist of polycrystals made up of different constituents, as shown in Fig. 2 and described in Table 1. The differences in stiffness and yield properties
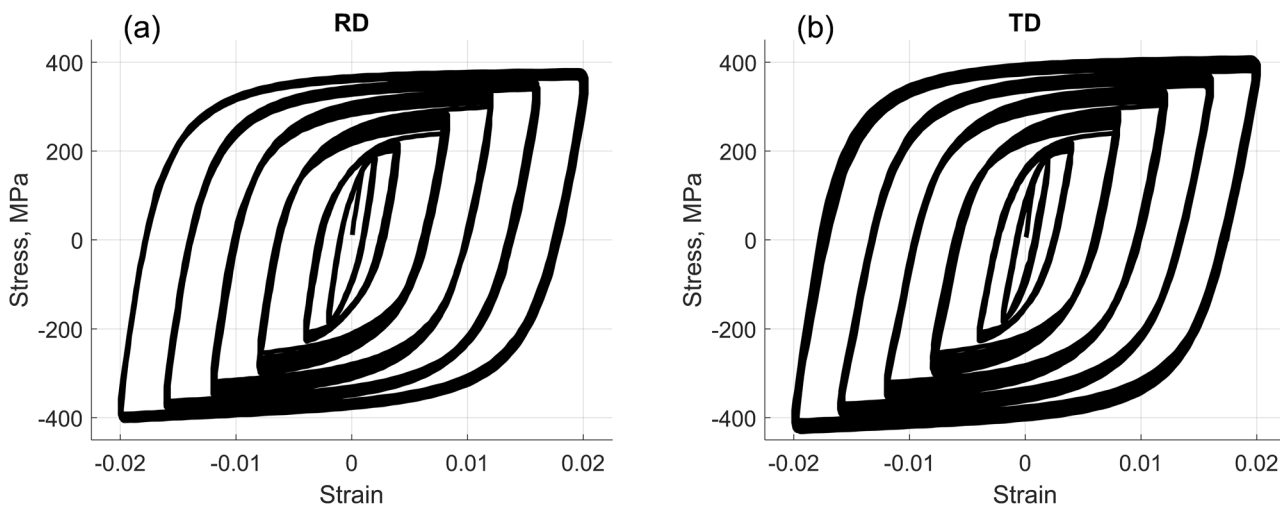
Fig. 9 Hysteresis loops at 300 °C for different strain amplitudes in (**a**) the rolling direction (RD) and (**b**) the transverse direction (TD)
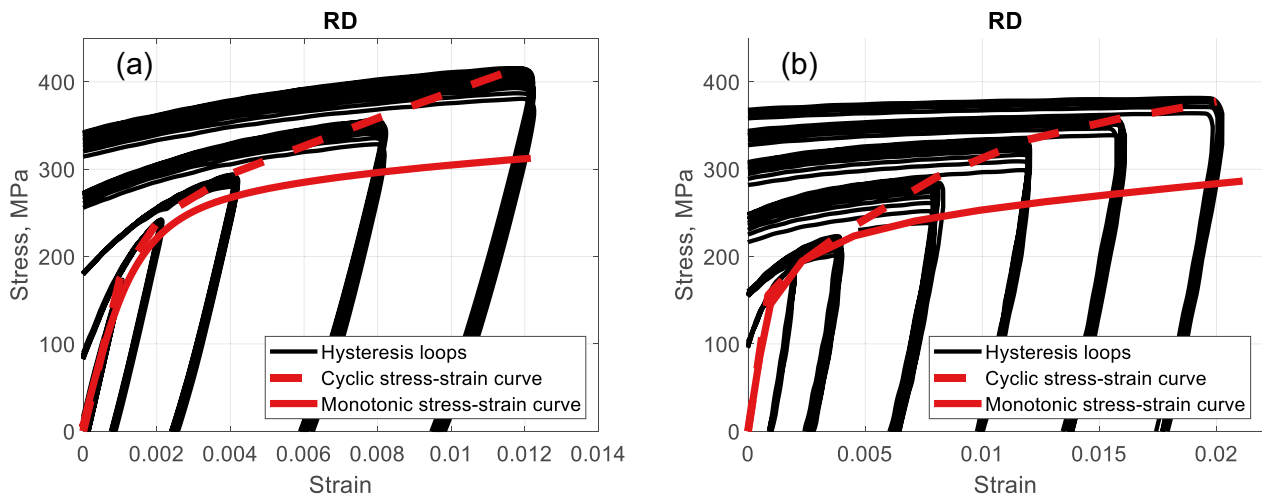
Fig. 10 Cyclic and monotonic stress-strain curves in the rolling direction at (**a**) room temperature and (**b**) 300 °C

among the constituents imply that each constituent undergoes different plastic straining when the material is loaded into the plastic regime. When the loading is reversed, this mismatch of the constituents means that some constituents again enter the plastic regime before others and this manifests itself in the macrolevel as the Bauschinger effect and thereby kinematic hardening [13].

The transition from elastic to plastic behavior is very smooth for 304L and therefore difficult to pinpoint. The monotonic yield strength, σ_{Y0}, in Table 3 would significantly overestimate the elastic range in the hysteresis loops. Hence, a lower cyclic yield strength, σ_Y, was fitted to the cyclic curves in Figs. 11 and 12 and this parameter is the only one that is independent of the strain amplitude. All parameters are based on optimized values by the least squares method performed in a previous study [45] for 316L at room temperature, which is similar to 304L. Manual fine-tuning of the parameters was then adopted to match the experimental results as accurately as possible. Apart from the yield strength, all parameters are dependent on the strain amplitude. Interpolation can be utilized to obtain the parameters for a specific strain amplitude. The initial value of the accumulated plastic strain, α, is only zero for the first strain amplitude of 0.2 %. For all other amplitudes, the initial accumulated plastic strain is non-zero due to the memory effects from previous strain cycles. Thus, there is a history

dependence on the hardening parameters since all hysteresis loops are obtained from a single specimen. However, the parameters for $\varepsilon_a \leq 0.4\%$ can be used independently in a low cycle fatigue analysis since the initial accumulated plastic strain is zero for $\varepsilon_a = 0.2\%$ and negligible for $\varepsilon_a = 0.4\%$. In addition, the initial condition values do not influence the stabilized hysteresis loops regardless of the strain amplitude. Thus, the stabilized curves are history-independent and this is attributed to the fact that they are determined from the kinematic hardening model, which is independent of the accumulated plastic strain, α. Hence, the parameters can still be used with high accuracy to perform low cycle fatigue analyses and predict damage without considering the history effects. For higher strain amplitudes, the hardening parameters can be extrapolated since a clear pattern is evident between the strain amplitudes and the hardening parameters. For variable amplitude loading, the largest occurring strain amplitude dictates the cyclic hardening behavior of the material when saturation is achieved at lower levels. The hardening parameter set for the maximum strain amplitude should always be used until a greater strain amplitude is reached. Hence, the parameters throughout an analysis should be dependent on the maximum strain amplitude occurring up to that point. The above-mentioned material model is unable to capture softening effects resulting in saturation at lower stress levels. It is also unable to describe non-uniform deformation of the yield surface. Experiments with 316L have shown that the surface depends heavily on the direction of loading [45]. In addition, the material model is solely dependent on the accumulated plastic strain although there is a clear dependency of the hardening parameters on the strain amplitude.

The proposed fatigue life prediction model in the form of a power law, see Eq. (24), successfully captures the correlation

Table 6 Ramberg-Osgood parameters for the cyclic stress-strain curves

		H' MPa	n'
RT	RD	2190	0.349
	TD	2190	0.340
300 °C	RD	1174	0.278
	TD	1203	0.268
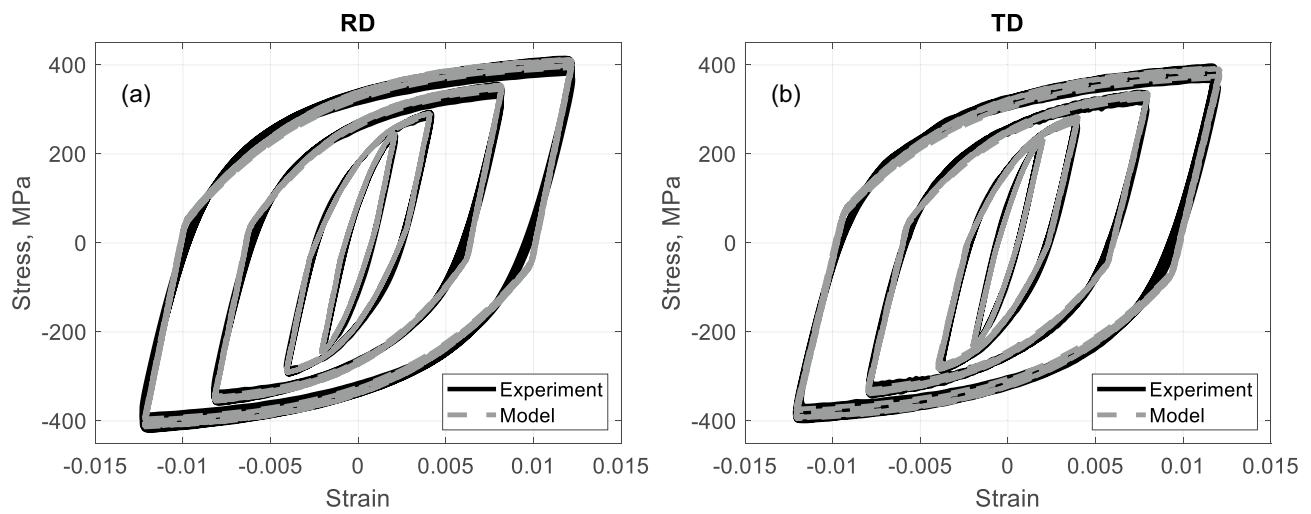
Fig. 11 Combined nonlinear kinematic and isotropic hardening model fit at room temperature in (**a**) the rolling direction and (**b**) the transverse direction
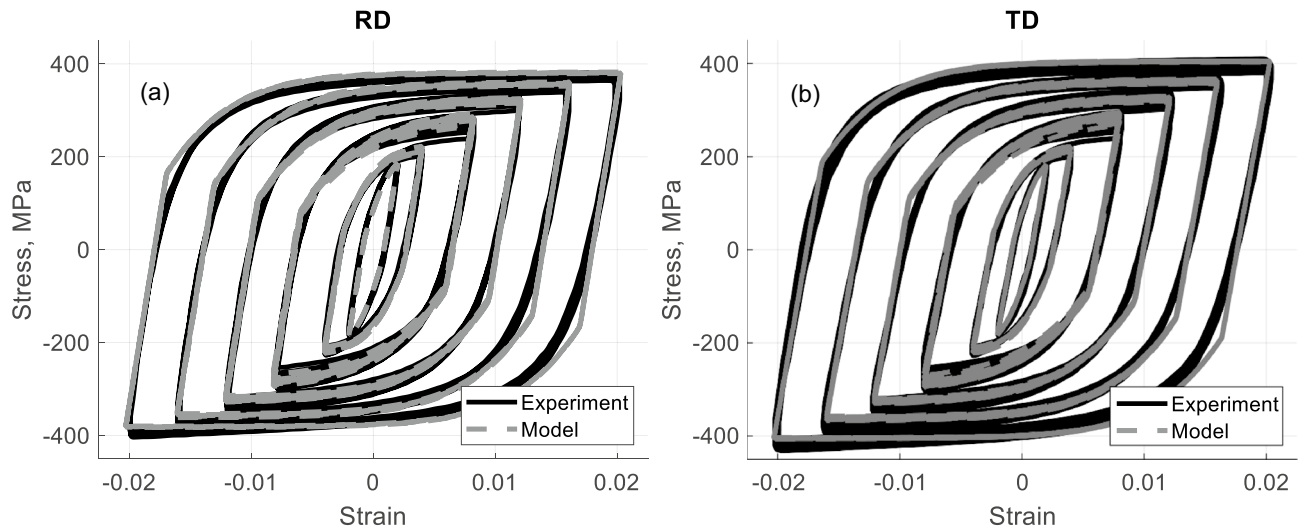
Fig. 12 Combined nonlinear kinematic and isotropic hardening model fit at 300 °C in (**a**) the rolling direction and (**b**) the transverse direction

Table 7 Kinematic and isotropic hardening parameters for different strain amplitudes at room temperature (RT) in the rolling direction (RD) and the transverse direction (TD)

RT	RD						TD					
	ε_a %	σ_Y MPa	σ_{sat} MPa	β	C_k GPa	γ_k	ε_a %	σ_Y MPa	σ_{sat} MPa	β	C_k GPa	γ_k
	0.2	100	15	30	240	1400	0.2	100	15	30	350	2500
	0.4	100	30	20	107	600	0.4	100	50	20	95	600
	0.8	100	100	8	43	250	0.8	100	100	8	40	250
	1.2	100	140	3	34	180	1.2	100	150	3	30	180

Table 8 Kinematic and isotropic hardening parameters for different strain amplitudes at 300 °C in the rolling direction (RD) and the transverse direction (TD)

300 °C	RD						TD					
	ε_a %	σ_Y MPa	σ_{sat} MPa	β	C_k GPa	γ_k	ε_a %	σ_Y MPa	σ_{sat} MPa	β	C_k GPa	γ_k
	0.2	100	15	30	125	1200	0.2	100	15	30	125	1200
	0.4	100	40	15	65	700	0.4	100	40	15	65	700
	0.8	100	105	5	27	250	0.8	100	105	5	27	250
	1.2	100	130	3	27	250	1.2	100	130	3	27	250
	1.6	100	165	2	27	250	1.6	100	165	2	27	250
	2.0	100	180	2	27	250	2.0	100	200	2	27	250
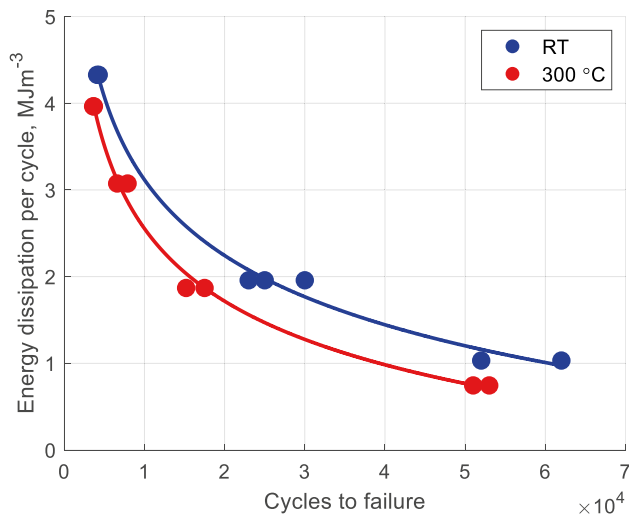
Fig. 13 Energy dissipation per cycle for the low cycle fatigue tests

Table 9 Parameters for the energy based fatigue life prediction model

	W_a MJm^{-3}	W_b MJm^{-3}	p
RT	33.540	-7.077	-0.1293
300 °C	39.360	-4.179	-0.1917

between energy dissipation and fatigue life, as shown in Fig. 13. The model is based on the energy density computed from the hysteresis area using the return mapping algorithm. The accumulated plastic strain could also be used to obtain a similar model. However, energy dissipation is favourable since it accounts for both accumulated plastic strain and strain hardening. The model could be used for estimating the fatigue life of variable amplitude loading as well by computing the dissipated energy for a specific block loading but further testing should be conducted for verification of the model. It is important to note that the model only considers loading cycles within the plastic deformation range and does not take into account damage caused by purely elastic loading cycles. As a result, there is a specific strain amplitude threshold that defines the validity of the model. However, due to the material's impressive fatigue limit near its yield strength, elastic cyclic loads have a lesser impact on the material's fatigue life. Consequently, the threshold closely aligns with the fatigue limit.

Conclusions

The hot rolled 304L stainless steel exhibits high isotropy in its mechanical properties, including tensile strength, fatigue performance, crack growth rates and cyclic plasticity, at both room and elevated temperature. The mechanical performance is

generally weaker at 300 °C. The nonlinear kinematic hardening model proposed by Armstrong-Frederick can be used in conjunction with the nonlinear isotropic hardening law proposed by Voce to successfully model the cyclic plasticity of the material using a von Mises radial return-mapping algorithm. However, the material model has some drawbacks, including the incapability of capturing softening effects, nonuniform deformation of the yield surface and dependence on strain amplitude. The radial return mapping algorithm can be used to determine the dissipated energy per cycle which together with fatigue testing has been used to propose a low cycle fatigue life prediction model at both temperatures.

Appendix A. Implicit backward Euler integration scheme

It proves convenient to introduce the auxiliary variable

$$\xi = \sigma - \frac{3}{2}q, \tag{A.1}$$

known as the relative stress, to address the numerical implementation of the constitutive models described above. The flow rule in Eq. (13), the evolution law in Eq. (16) and the kinematic hardening law in Eq. (17) can now be written in the discrete form

$$\begin{cases} \varepsilon_{n+1}^p = \varepsilon_n^p + \Delta\lambda \, \text{sign}(\xi_{n+1}) \\ \alpha_{n+1} = \alpha_n + \Delta\lambda \\ q_{n+1} = \frac{1}{1+\gamma_k\Delta\lambda}q_n + \frac{2}{3}\frac{1}{1+\gamma_k\Delta\lambda}C_k\Delta\lambda \, \text{sign}(\xi_{n+1}) \end{cases}, \tag{A.2}$$

where

$$\xi_{n+1} = \sigma_{n+1} - \frac{3}{2}q_{n+1}, \tag{A.3}$$

and $\Delta\lambda$ is a Lagrange multiplier which is the algorithmic counterpart of the consistency parameter, λ. The return-mapping algorithm initiates by first considering an auxiliary state, in the form of a purely elastic trial step, which may not, and in general will not, correspond to any actual, physically admissible state unless the incremental process is elastic. Hence, this step is called the elastic predictor and is defined by the formulas

$$\begin{cases} \sigma_{n+1}^{\text{trial}} = E(\varepsilon_{n+1} - \varepsilon_n^p) \\ \xi_{n+1}^{\text{trial}} = \sigma_{n+1}^{\text{trial}} - \frac{3}{2}q_n \\ f_{n+1}^{\text{trial}} = \left|\xi_{n+1}^{\text{trial}}\right| - (\sigma_Y + \sigma_{\text{sat}}[1 - \exp(-\beta\alpha_n)]) \end{cases}, \tag{A.4}$$

where the integration technique is based on a strain-driven approach where

$$\varepsilon_{n+1} = \varepsilon_n + \Delta\varepsilon_n. \tag{A.5}$$

Eq. (A.4) together with the initial conditions $\{\varepsilon_n^p, q_n, \alpha_n\}$ solely determines the trial state. The trial state is admissible and thus a solution to the problem only if it satisfies the stress-strain relationship, the flow rule and the hardening laws and especially the Karush-Kuhn-Tucker conditions which leads us to the following criterion

$$f_{n+1}^{\text{trial}} \begin{cases} \leq 0 \rightarrow \text{elastic step } \Delta\lambda = 0, \\ > 0 \rightarrow \text{plastic step } \Delta\lambda > 0. \end{cases} \tag{A.6}$$

The process is incrementally plastic for the case in which $f_{n+1}^{\text{trial}} > 0$ and the trial state cannot be a solution to the incremental problem since $(\sigma_{n+1}^{\text{trial}}, \alpha_n, q_n)$ violates the constraint condition $f(\sigma, \alpha, q) \leq 0$. Thus, the consistency parameter $\Delta\lambda > 0$, which enforces $f_{n+1} = 0$, has to be determined in order to obtain $\sigma_{n+1} \neq \sigma_{n+1}^{\text{trial}}$. This results in the so called plastic corrector step which completes the return-mapping algorithm. The stress value σ_{n+1} can be expressed as

$$\sigma_{n+1} = \sigma_{n+1}^{\text{trial}} - \Delta\lambda E \, \text{sign}(\xi_{n+1}), \tag{A.7}$$

where both $\Delta\lambda$ and $\text{sign}(\xi_{n+1})$ need to be determined by use of the condition $f_{n+1} = 0$ where

$$f_{n+1} = |\xi_{n+1}| - (\sigma_{\text{Y}} + \sigma_{\text{sat}}[1 - \exp(-\beta\alpha_n)]). \tag{A.8}$$

Here, the unknown relative stress ξ_{n+1} can be expressed as

$$\begin{aligned} \xi_{n+1} = \sigma_{n+1}^{\text{trial}} - \Delta\lambda E \, \text{sign}(\xi_{n+1}) - \frac{3}{2}\frac{1}{1+\gamma_k\Delta\lambda} \\ \left(q_n + \frac{2}{3}C_k\Delta\lambda \, \text{sign}(\xi_{n+1})\right), \end{aligned} \tag{A.9}$$

by use of Eqs. (A.1), (A.2) and (A.7).

Appendix B. Determination of the sign of the auxiliary variable

Rearranging Eq. (A.9) gives

$$\begin{aligned} \xi_{n+1} = \xi_{n+1}^{\text{trial}} + \left(1 - \frac{1}{1+\gamma_k\Delta\lambda}\right)\frac{3}{2}q_n \\ - \left(E + C_k\frac{1}{1+\gamma_k\Delta\lambda}\right)\Delta\lambda \, \text{sign}(\xi_{n+1}). \end{aligned} \tag{B.1}$$

Utilizing factorization and that $\text{sign}(\xi_{n+1}) = \xi_{n+1}/|\xi_{n+1}|$, we have

$$\begin{aligned} \left[|\xi_{n+1}| + E\Delta\lambda + C_k\frac{\Delta\lambda}{1+\gamma_k\Delta\lambda}\right]\text{sign}(\xi_{n+1}) \\ = \xi_{n+1}^{\text{trial}} + \left(1 - \frac{1}{1+\gamma_k\Delta\lambda}\right)\frac{3}{2}q_n. \end{aligned} \tag{B.2}$$

Here, the terms in the brackets on the left hand side are all positive values which leads to the conclusion that $\text{sign}(\xi_{n+1})$ must agree with the sign of the right hand side according to

$$\text{sign}(\xi_{n+1}) = \frac{\xi_{n+1}^{\text{trial}} + \left(1 - \frac{1}{1+\gamma_k\Delta\lambda}\right)\frac{3}{2}q_n}{\left|\xi_{n+1}^{\text{trial}} + \left(1 - \frac{1}{1+\gamma_k\Delta\lambda}\right)\frac{3}{2}q_n\right|}, \tag{B.3}$$

which now leaves $\Delta\lambda$ as the only unknown parameter. The absolute value of the relative stress, $|\xi_{n+1}|$, is now given by

$$|\xi_{n+1}| = \left|\xi_{n+1}^{\text{trial}} + \left(1 - \frac{1}{1+\gamma_k\Delta\lambda}\right)\frac{3}{2}q_n\right| - \left(E + C_k\frac{1}{1+\gamma_k\Delta\lambda}\right)\Delta\lambda. \tag{B.4}$$

Appendix C. Newton's method to determine consistency parameter

The yield condition in Eq. (A.8) can be rewritten to

$$\begin{aligned} f_{n+1} = \left|\xi_{n+1}^{\text{trial}} + \left(1 - \frac{1}{1+\gamma_k\Delta\lambda}\right)\frac{3}{2}q_n\right| - \left(E + C_k\frac{1}{1+\gamma_k\Delta\lambda}\right)\Delta\lambda \\ - (\sigma_{\text{Y}} + \sigma_{\text{sat}}[1 - \exp(-\beta(\alpha_n + \Delta\lambda))]) = 0. \end{aligned} \tag{C.1}$$

Eq. (C.1) is effectively solved for $\Delta\lambda$ by a Newton iterative procedure. The derivative of the yield function with respect to $\Delta\lambda$ is given by

$$\begin{aligned} \mathrm{d}f_{n+1} = \left(\xi_{n+1}^{\text{trial}} + \left(1 - \frac{1}{1+\gamma_k\Delta\lambda}\right)\frac{3}{2}q_n\right) \\ \frac{\frac{3}{2}\frac{q_n\gamma_k}{(1+\gamma_k\Delta\lambda)^2}}{\left|\xi_{n+1}^{\text{trial}} + \left(1 - \frac{1}{1+\gamma_k\Delta\lambda}\right)\frac{3}{2}q_n\right|} - E + \frac{C_k}{1+\gamma_k\Delta\lambda}\left[\frac{\gamma_k\Delta\lambda}{1+\gamma_k\Delta\lambda} - 1\right] \\ - \sigma_{\text{sat}}\beta\exp(-\beta(\alpha_n + \Delta\lambda)), \end{aligned} \tag{C.2}$$

and the iterative Newton-Raphson solution is given by

$$\Delta\lambda^{n+1} = \Delta\lambda^n - \frac{f_{n+1}}{\mathrm{d}f_{n+1}}. \tag{C.3}$$

Declarations

Conflict of Interest On behalf of all authors, the corresponding author declares that there are no known competing financial interests or personal relationships that could have appeared to influence the work reported in this paper.

References

1. IAEA (2018) (NP-T-3.20) Buried and underground piping and tank ageing management for nuclear power plant. 35–7
2. Coffin LF (1954) A study of the effects of cyclic thermal stresses on a ductile metal. Trans ASME 76:931–50
3. Manson SS (1965) Fatigue: A complex subject—Some simple approximations. Exp Mech 5:193–226. https://doi.org/10.1007/bf02321056
4. Basquin OH (1910) The Exponential Law of Endurance Tests. ASTM Proc 10:625–30
5. Ramberg W, Osgood WR (1943) Description of stress-strain curves by three parameters
6. Paris P, Gomez M, Paris WA Gomez PC, Anderson MP WEP (1961) A rational analytic theory of fatigue. Trend Eng 13:9–14
7. Prager W (1956) A New Method of Analyzing Stresses and Strains in Work-Hardening Plastic Solids. J Appl Mech 23:493–6. https://doi.org/10.1115/1.4011389
8. Ziegler H (1958) A modification of prager's hardening rule* 55–65
9. Voce E (1948) The relationship between stress and strain for homogeneous deformation. J Inst Met 74:537–62
10. Mróz Z (1967) On the description of anisotropic workhardening. J Mech Phys Solids 15:163–75. https://doi.org/10.1016/0022-5096(67)90030-0
11. Ohno N, Wang JD (1993) Kinematic hardening rules with critical state of dynamic recovery, part I: formulation and basic features for ratchetting behavior. Int J Plast 9:375–90. https://doi.org/10.1016/0749-6419(93)90042-O
12. Frederick CO, Armstrong PJ (1966) A mathematical representation of the multiaxial Bauschinger effect. Mater High Temp 24:1–26
13. Ottosen NS, Ristinmaa M (2005) Nonlinear kinematic hardening Laws. Mech Const Model, Elsevier; p. 321–55. https://doi.org/10.1016/b978-008044606-6/50013-8
14. Chaboche JL (1989) Constitutive equations for cyclic plasticity and cyclic viscoplasticity. Int J Plast 5:247–302. https://doi.org/10.1016/0749-6419(89)90015-6
15. Bemfica C, Carneiro L, Mamiya EN, Castro FC (2019) Fatigue and cyclic plasticity of 304L stainless steel under axial-torsional loading at room temperature. Int J Fatigue 125:349–61. https://doi.org/10.1016/j.ijfatigue.2019.04.009
16. Grigorescu AC, Hilgendorff PM, Zimmermann M, Fritzen CP, Christ HJ (2016) Cyclic deformation behavior of austenitic Cr–Ni-steels in the VHCF regime: Part I - Experimental study. Int J Fatigue 93:250–60. https://doi.org/10.1016/j.ijfatigue.2016.05.005
17. Taleb L, Cailletaud G, Saï K (2014) Experimental and numerical analysis about the cyclic behavior of the 304L and 316L stainless steels at 350 °C. Int J Plast 61:32–48. https://doi.org/10.1016/j.ijplas.2014.05.006
18. Taleb L, Hauet A (2009) Multiscale experimental investigations about the cyclic behavior of the 304L SS. Int J Plast 25:1359–85. https://doi.org/10.1016/j.ijplas.2008.09.004
19. Lindström T, Ewest D, Simonsson K, Eriksson R, Lundgren JE, Leidermark D (2020) Constitutive model of an additively manufactured ductile nickel-based superalloy undergoing cyclic plasticity. Int J Plast 132:1–15. https://doi.org/10.1016/j.ijplas.2020.102752
20. Zhou J, Sun Z, Kanouté P, Retraint D (2018) Experimental analysis and constitutive modelling of cyclic behaviour of 316L steels including hardening/softening and strain range memory effect in LCF regime. Int J Plast 107:54–78. https://doi.org/10.1016/j.ijplas.2018.03.013
21. Bui-Quoc T (1975) High-temperature fatigue-life estimation: extension of a unified theory 219–25. https://doi.org/10.1007/bf02319426
22. Bui-Quoc T, Biron A (1978) Comparison of low-cycle fatigue results with axial and diametral extensometers. Pap SESA Present Spring Meet, Wichita, Kans 127–33. https://doi.org/10.1007/bf02324144
23. Sciammarella CA, Rao MPK (1979) Failure analysis of stainless steel at elevated temperatures. Exp Mech 19:389–98. https://doi.org/10.1007/bf02324504
24. Tiruvengadam A, Conn AF (1971) On high-frequency fatigue and dynamic properties at elevated temperature. Exp Mech 11:315–20. https://doi.org/10.1007/bf02320585
25. Slot T, Stentz RH (1968) Experimental procedures for low-cycle-fatigue research at high temperatures. Exp Mech 8:107–14. https://doi.org/10.1007/bf02326104
26. Mohanty S, Soppet WK, Barua B, Majumdar S, Natesan K (2017) Modeling the Cycle-Dependent Material Hardening Behavior of 508 low Alloy Steel. Exp Mech 57:847–55. https://doi.org/10.1007/s11340-017-0278-y
27. Lawton CW (1968) High-temperature low-cycle fatigue: A summary of industry and code work. Exp Mech 8:257–66. https://doi.org/10.1007/bf02327022
28. Chang CS, Pimbley WT, Conway HD (1968) An analysis of metal fatigue based on hysteresis energy - Main purpose of investigation is to extend Halford's work on low-cycle fatigue to the medium- and high-cycle range by including the concept of an endurance limit. Exp Mech 8:133–7. https://doi.org/10.1007/BF02326108
29. Bai Y, Nardi DC, Zhou X, Picón RA, Flórez-López J (2021) A new comprehensive model of damage for flexural subassemblies prone to fatigue. Comput Struct 256. https://doi.org/10.1016/j.compstruc.2021.106639
30. Niu X, Zhu SP, He JC, Luo C, Wang Q (2023) Probabilistic and defect tolerant fatigue assessment of AM materials under size effect. Eng Fract Mech 277. https://doi.org/10.1016/j.engfracmech.2022.109000
31. Guo K, Gou G, Lv H, Shan M (2022) Jointing of CFRP/5083 Aluminum Alloy by Induction Brazing: Processing, Connecting Mechanism, and Fatigue Performance. Coatings 12. https://doi.org/10.3390/coatings12101559
32. Li XK, Zhu SP, Liao D, Correia JAFO, Berto F, Wang Q (2022) Probabilistic fatigue modelling of metallic materials under notch and size effect using the weakest link theory. Int J Fatigue 159. https://doi.org/10.1016/j.ijfatigue.2022.106788
33. Svensk standard SS-EN 10088-1:2014. Stockholm: 2014.

34. ASTM E8 (2010) ASTM E8/E8M standard test methods for tension testing of metallic materials 1. Annu B ASTM Stand 4:1–27. https://doi.org/10.1520/E0008

35. Croné P, Zhou T, Hedström P, Odqvist J, Gudmundson P, Faleskog J (2022) Continuum plasticity modelling of work hardening for precipitation-hardened martensitic steel guided by atom probe tomography. Mater Des 215:110463. https://doi.org/10.1016/j.matdes.2022.110463

36. ASTM E606-21 (n.d.) Standard test method for strain-controlled fatigue testing. https://doi.org/10.1520/E0606

37. Little RE, Jebe EH (1975) Statistical Design of Fatigue Experiments. Wiley corp, New York, pp 215–220

38. Little RE (1975) Manual on statistical planning and analysis for fatigue experiments. ASTM STP 588:54–60

39. ASTM E647−13 (2014) Standard test method for measurement of fatigue crack growth rates. Am Soc Test Mater 1–50. https://doi.org/10.1520/E0647-15E01.2

40. Bridgman PW (1944) The stress distribution at neck of tension specimen. Amercian Soc Met - Trans 32:553–72

41. Davidenkov NN, Spiridonova NI (1946) Mechanical methods of testing analysis of the state of stress in the neck of a tension test specimen. Proc Am Soc Test Mater 46:1147–58

42. Wilkins ML (1964) Calculation of elastic-plastic flow. Methods Comput Phys 3

43. Simo JC, Hughes TJR (1999) Computational inelasticity. Springer 7. https://doi.org/10.1016/s0898-1221(99)90277-8

44. De Angelis F, Taylor RL (2015) An efficient return mapping algorithm for elastoplasticity with exact closed form solution of the local constitutive problem. Eng Comput (Swansea, Wales) 32:2259–91. https://doi.org/10.1108/EC-06-2014-0138

45. Van Eeten P, Nilsson F (2006) Constant and variable amplitude cyclic plasticity in 316L stainless steel. J Test Eval 34:298–311